



# 1 **Temporal changes in rainfall intensity-duration thresholds for post-** 2 **wildfire flash floods and sensitivity to spatiotemporal distributions of** 3 **rainfall**

4 Tao Liu<sup>1,2</sup>, Luke A. McGuire<sup>1</sup>, Nina Oakley<sup>3</sup>, Forest Cannon<sup>3</sup>

5 <sup>1</sup>Department of Geosciences, University of Arizona, Tucson, AZ 85721-0011, USA

6 <sup>2</sup>Department of Hydrology and Atmospheric Sciences, University of Arizona, Tucson, AZ 85721-0011, USA

7 <sup>3</sup>Center for Western Weather and Water Extremes, Scripps Institution of Oceanography, University of California, San Diego,  
8 La Jolla, CA, USA

9 *Correspondence to:* Tao Liu (liutao@arizona.edu)

10 **Abstract.** Rainfall intensity-duration (ID) thresholds are commonly used to assess flash flood potential downstream of burned  
11 watersheds. High-intensity and/or long-duration rainfall is required to generate flash floods as landscapes recover from fire,  
12 but there is little guidance on how thresholds change as a function of time since burning. Here, we force a hydrologic model  
13 with radar-derived precipitation to estimate ID thresholds for post-fire flash floods in a 41.5 km<sup>2</sup> watershed in southern  
14 California, USA. Prior work in this study area constrains temporal changes in hydrologic model parameters, allowing us to  
15 estimate temporal changes in ID thresholds. Results indicate that ID thresholds increase by more than a factor of 2 from post-  
16 fire year 1 to post-fire year 5. Thresholds based on averaging rainfall intensity over durations of 30-60 minutes perform better  
17 than those that average rainfall intensity over shorter time intervals. Moreover, thresholds based on the 75<sup>th</sup> percentile of radar-  
18 derived rainfall intensity over the watershed perform better than thresholds based on the 25<sup>th</sup> or 50<sup>th</sup> percentile of rainfall  
19 intensity. Results demonstrate how hydrologic models can be used to estimate changes in ID thresholds following disturbance  
20 and provide guidance on the rainfall metrics that are best suited for predicting post-fire flash floods.

21



## 22 **1 Introduction**

23 Heightened hydrologic responses are common within and downstream of recently burned areas, resulting in an increased  
24 likelihood of flash floods. Rainfall intensity-duration (ID) thresholds are commonly used to assess the potential for flash floods  
25 (Moody and Martin, 2001; Cannon et al., 2008). Many past studies aimed at defining thresholds for flash floods focus on the  
26 first 1-2 years following fire (Cannon et al., 2008; Wilson et al., 2018). Since the hydrologic impacts of fire are transient,  
27 rainfall ID thresholds associated with flash floods are likely to change as a watershed recovers (Ebel and Martin, 2017; Ebel  
28 and Moody, 2017; Moreno et al, 2019; Ebel, 2020). It may take more than a decade for hydrologic responses to return to pre-  
29 fire levels, yet there is limited guidance on how the magnitude and utility of rainfall ID thresholds change with time since  
30 burning. Given the increased frequency and size of fire in many geographic and ecological zones (e.g. Gillett et al., 2004;  
31 Westerling et al., 2006; Kitzberger et al., 2017), it is of growing importance to quantify the best metrics for assessing flash-  
32 flood potential in the immediate aftermath of fire as well as how these metrics change throughout the recovery process (e.g.  
33 Ebel, 2020).

34  
35 Rainfall ID thresholds for flash floods are typically defined using historic data that relates rainfall over different intensities  
36 and durations to an observed hydrologic response, namely the presence or absence of flooding (e.g. Cannon et al., 2008). Due  
37 to the stochastic nature of rainfall over burned areas and limited observations throughout the recovery process, there is a  
38 paucity of data that can be used to derive empirical thresholds for flash flooding beyond one year of recovery. Hazards  
39 associated with flash flooding, however, may exist downstream of burned areas well beyond one year of recovery. Wildfire  
40 alters rainfall-runoff partitioning and flood routing by incinerating vegetation and reducing interception capacity (Stoof et al.,  
41 2012, Saksa et al., 2020), decreasing hydraulic roughness, and reducing soil infiltration capacity (Larsen et al., 2009, Ebel and  
42 Moody, 2013). Reductions in infiltration capacity are often attributed to fire-induced soil water repellency (Ebel and Moody,  
43 2013), which is generally strongest immediately following a fire and then decays over time scales ranging from one year to  
44 more than five years (Dyrness, 1976; Huffman et al., 2001; Larsen et al., 2009), though surface soil sealing (Larsen et al.,  
45 2009) and hyper-dry conditions (Moody and Ebel, 2012) are also known to play important roles. Vegetation recovery, which  
46 may influence temporal changes in hydraulic roughness and canopy interception, can take five years or longer. Cannon et al.  
47 (2008) collected sufficient data over a two-year time period following fire in southern California, USA, to define separate  
48 rainfall ID thresholds for post-fire debris flows and flash floods in the first- and second-years following fire. They found that  
49 the ID thresholds for flash floods and debris flows may increase by as much as 25 mm/h after one year of recovery, a change  
50 that they attributed to a combination of vegetation growth and sediment removal as a result of rainstorms during the first post-  
51 fire year.

52  
53 Rainfall ID thresholds are often defined over a range of durations, though averaging rainfall intensity over a particular duration  
54 may provide a more reliable threshold. Post-fire hydrological response in the first few years is often best related to rainfall



55 intensity over short durations (less than 60 min) (Staley et al., 2017; Moody and Martin, 2001). In their efforts to define rainfall  
56 ID thresholds for post-fire debris flows, Staley et al. (2013) showed that averaging rainfall intensities over durations between  
57 15 minutes and 60 minutes resulted in thresholds that performed better relative to those associated with longer durations. One  
58 potential explanation for this observation is that post-fire debris flows are often triggered by runoff in steep, low-order  
59 drainages, which both Kean et al. (2011) and Raymond et al. (2020) have found to be highly correlated with rainfall intensities  
60 averaged over similarly short time intervals (10-15 minutes). Moody and Martin (2001) have also documented a substantial  
61 increase in peak discharge following wildfire once the 30-minute rainfall intensity ( $I_{30}$ ) crossed a threshold value, suggesting  
62 that  $I_{30}$  may be a consistent predictor of flash flood activity in recently burned watersheds. Moody and Martin (2001) suggest  
63 that peak  $I_{30}$  can be used to set the threshold for early-warning flood systems. The optimal duration for defining post-fire flash  
64 floods thresholds, as well as how it may change with time, remains relatively unexplored.

65  
66 Rain gage records are typically used to derive rainfall ID thresholds for flash flood and post-fires debris flows (Staley et al.,  
67 2013; Staley et al., 2017). Post-fire debris flows, however, tend to initiate in small ( $<1 \text{ km}^2$ ), steep watersheds. In these small  
68 watersheds, the rainfall intensity responsible for initiating a debris flow can be characterized by a single rain gage installed  
69 near the initiation zone. Flash floods differ in that they tend to occur at larger spatial scales where rainfall is spatially variable  
70 and may not be adequately characterized by data from a single rain gage. Radar-derived precipitation estimates, which can  
71 provide high spatiotemporal resolution of rainfall intensity, present opportunities to develop basin-specific thresholds for post-  
72 fire flash floods. However, high spatiotemporal variability in rainfall intensity also brings new challenges when employing  
73 radar-derived precipitation in flood warning practice. In particular, what is the best way to summarize spatially and temporally  
74 variable rainfall intensity information with a single metric that can be used as a threshold? How does hydrological recovery  
75 following fire influence the generation of flash floods and the metrics that are best suited for their prediction? Data-driven  
76 approaches to answering these and related questions may be hampered by limited monitoring of post-fire hydrologic response  
77 throughout the recovery period and the stochastic occurrence of rainfall over burned areas, which limits opportunities for  
78 observations. Given a well-constrained hydrologic model that accounts for changes associated with post-fire recovery, it is  
79 possible to use numerical experiments to understand relationships between time since burning, the spatiotemporal patterns of  
80 rainfall over a watershed, and the occurrence of flash floods.

81  
82 Here, we use realistic patterns of spatially and temporally varying radar-derived rainfall over a  $41.5 \text{ km}^2$  watershed in the San  
83 Gabriel Mountains of southern California, USA, to (1) determine the optimal method to define a rainfall ID threshold for flash  
84 floods, and (2) identify changes in rainfall ID thresholds for flash floods as a function of time since burning. The watershed,  
85 which we refer to as the upper Arroyo Seco, burned during the 2009 Station Fire (USDA Forest Service, 2009). Liu et al.  
86 (2021) used rain and stream gage data collected at different times following the fire to calibrate the KINEROS2 hydrologic  
87 model for this watershed, enabling them to quantify temporal changes in model parameters as a function of time since burning.  
88 Combining this calibrated model with spatially explicit, radar-derived estimates of rainfall intensity during 34 rainstorms, we



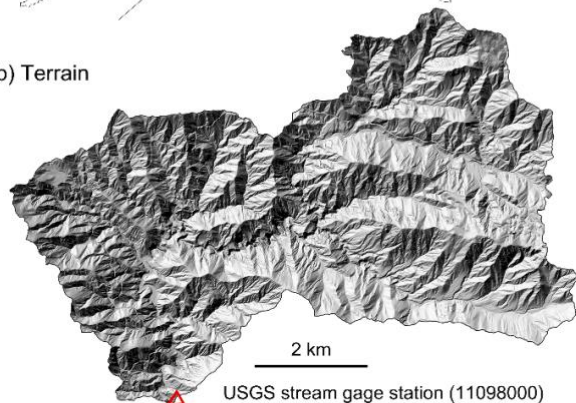
89 explore the utility of different rainfall ID metrics as flash flood thresholds and quantify temporal changes in those thresholds  
90 through the first five years of recovery. Results provide insight into the magnitude of temporal changes in flash flood thresholds  
91 in the densely populated, fire-prone region of southern California. More generally, results support the development of early  
92 warning systems for flash floods by identifying specific metrics that can be computed using spatially variable rainfall intensity  
93 estimates to assess the potential for flash flooding.

## 94 2 Study Area

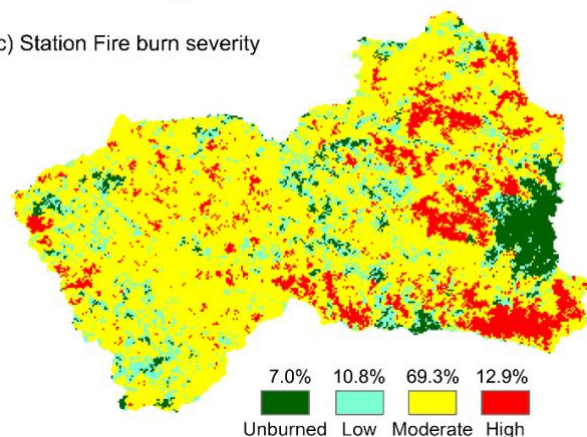
(a) Upper Arroyo Seco in California, USA



(b) Terrain



(c) Station Fire burn severity



95  
96 **Figure 1: Modified from figure 1 in Liu et al. (2021) (a) The location of the upper Arroyo Seco watershed within California. The red**  
97 **triangle indicates the location of the USGS stream gage (11098000); (b) Shaded relief showing the study watershed with the USGS**



98 stream gage (red triangle; 34°13'20", -118°10'36"); (c) Soil burn severity for the 2009 Station fire. Burn severity percentages are for  
99 planform area within each category.

100

101 The upper Arroyo Seco watershed drains the 41.5 km<sup>2</sup> area above USGS stream gage station (11098000) near Pasadena in the  
102 San Gabriel Mountains (Figure. 1). The upper Arroyo Seco was burned in the August-October 2009 Station Fire, which burned  
103 more than 80% of the watershed at moderate to high soil burn severity (USDA Forest Service, 2009). Dominant shrubs and  
104 chaparral, such as chamise (*Adenostoma fasciculatum*) and manzanita (*Arctostaphylos spp.*), were completely consumed with  
105 severe soil heating in isolated patches throughout many areas burned at moderate to high severity (USDA Forest Service,  
106 2009). Soils in this area are typically sand and silty-sand textured and thin (<1 m) with partial exposure of bedrock (Staley et  
107 al., 2014). The majority of rainfall in the study area typically occurs in the cool season, between December and March, while  
108 warm, dry conditions dominate from April to early November. The San Gabriel Mountains also experience some of the most  
109 frequent short-duration, high-intensity rainfall in the state (Oakley et al. 2018a).

110

111 Due to wildfire-induced changes in surface conditions, including canopy cover and soil-hydraulic properties, runoff generation  
112 in the first year following the fire was likely dominated by infiltration excess overland flow (Schmidt et al., 2011, Liu et al.,  
113 2021). Enhanced soil water repellency (SWR), which helps promote low infiltration capacity, and extensive dry ravel, which  
114 loads channels with fine-grained hillslope sediment, are both commonly observed after fires in the San Gabriel Mountains  
115 (e.g., Watson and Letey, 1970; Hubbert and Oriol, 2005; Lamb et al., 2011; Hubbert et al., 2012). Rengers et al. (2019)  
116 calibrated a hydrologic model using data from small watersheds (0.01-2 km<sup>2</sup>) burned by the Station Fire and found relatively  
117 low values for saturated hydraulic conductivity ( $K_s$ ), generally between 2-10 mm/h. These results are consistent with values  
118 for saturated hydraulic conductivity inferred by Liu et al. (2021) via model calibration in the upper Arroyo Seco watershed.  
119 The impact of dry ravel, which reduces grain roughness in the channel network, and reduced vegetation density led to estimates  
120 of Manning's  $n$  in the channels of the upper Arroyo Seco of approximately 0.09 s m<sup>-1/3</sup> in the first year following fire (Liu et  
121 al., 2021). These hydrologic changes led to widespread flooding and debris flows during multiple rainstorms in the first winter  
122 after the fire (Kean et al., 2011; Oakley et al., 2017). As hydrologic recovery began over the next several years, the watershed-  
123 scale  $K_s$  and Manning's  $n$  generally increased and likely started to mitigate the flash flood risk (Liu et al., 2021).

## 124 3 Data and Methods

### 125 3.1 Radar-derived precipitation

126 We sought to identify storms in the study area that produced moderate-to-high intensity rainfall to use as inputs to a hydrologic  
127 model to simulate flood responses. Storm events were selected within the period for which observations are archived for the



128 two operational NWS Next-Generation Weather Radar installations (NEXRAD; NOAA 1991) that cover the study area,  
129 KSOX, (Santa Ana), and KVTX (Ventura). Though archives for the radars begin in 1997 and 1995, respectively.

130  
131 We compiled storm events starting with those known to have produced high intensity rainfall and a debris flow response in  
132 the San Gabriel Mountains (e.g., Table 1 in Oakley et al. 2017) as well as other storms that produced high-intensity rainfall in  
133 the region (e.g., Oakley et al. 2018b, Cannon et al. 2018). We then used hourly rainfall observations from the Clear Creek  
134 (2002-present), San Rafael Hills (2005-present), and Heninger Flats (2010-present) Remote Automated Weather Stations  
135 (RAWS, acquired from [raws.dri.edu](http://raws.dri.edu)) as indicator gages for the study area. This further limited us to post-2002 events outside  
136 of the literature. All gages are <10 km from the watershed of interest; there were no long-record gages within the watershed.  
137 We used 15 mm/h as a threshold for moderate to high intensity rainfall and extracted all events from the gauge record meeting  
138 or exceeding this value to develop a list of events of interest. We reviewed the radar data for these events at which point some  
139 of the selected events could not be utilized due to radar outages or poor data quality. This exercise presented us with 34 storm  
140 events (Table S1).

141  
142 Various atmospheric processes may contribute to generation of moderate-to-high rainfall intensities (e.g., Oakley et al. 2017),  
143 resulting in differing spatial and temporal precipitation patterns over a burn area. To ensure the events selected captured  
144 variability in spatial and temporal precipitation characteristics, we evaluated the spatial characteristics of the events. We found  
145 rainfall patterns could generally be categorized into four main spatial patterns at the scale of several tens of kilometers: (1) a  
146 broad pattern, a contiguous area of moderate-to-high intensity precipitation (>45 dBZ) spanning tens of kilometers; (2) a  
147 scattered pattern with numerous cells of moderate to high precipitation that are not spatially continuous; (3) an isolated pattern,  
148 with one to a few isolated cells of moderate-to-high intensity rainfall separated by non-precipitating areas several to tens of  
149 kilometers in extent; (4) a narrow cold frontal rainband (NCFR)—a north-south oriented narrow band (~3-5 km wide, tens to  
150 100 km in length) of very high intensity rainfall (e.g., Oakley et al. 2018b; Cannon et al. 2020; Figure S1 in Supplement). At  
151 the <10 km horizontal scale (the scale of the watershed), it was harder to identify meaningful patterns and distinctions, though  
152 the larger scale signals imply varying spatial and temporal patterns of precipitation as each pass over the watershed. A table  
153 of storm events and their characteristics is available in Table S1 in the Supplement.

154  
155 An approximate start and end time were determined for each event using the Clear Creek RAWS gauge as an indicator. Start  
156 time was determined by identifying the time of maximum 1h rainfall in the event and going back in time to the first of three  
157 consecutive hours of >1.5 mm/h precipitation. The end of an event was determined as the last hour where precipitation dropped  
158 below 3 mm/h for at least two consecutive hours.

159



160 Level-II base reflectivity (<https://www.ncdc.noaa.gov/wct/>) between the start and end time of each event was downloaded  
161 from both the KSOX and KVTX radars. The data were used to generate spatially-distributed precipitation over the study area.  
162 Radar imagery concurrent with the gauge-based record of high intensity rainfall events was converted to a composite maximum  
163 reflectivity product at 250 m spatial and 5-minute temporal resolution. Conversion of radar reflectivity to rain rate required  
164 the application of an empirically derived reflectivity (Z) to rain rate (R) relationship (e.g. Marshall and Palmer 1948). The Z-  
165 R relationship is conventionally represented by the equation  $Z = aR^b$ , which includes parameters a and b to account for  
166 variations in precipitation for a given reflectivity arising from differences in the drop size distribution. Due to the lack of  
167 previous studies investigating Z-R relationships in precipitating conditions over the region of interest, there are no standard a  
168 and b parameters to apply to the reflectivity data analyzed here. Thus, five well-known and previously published Z-R  
169 relationships were applied to the gridded reflectivity values. Supplement S3 lists the different Z-R relationships applied here  
170 and the general conditions for which they are suitable. Although the Z-R relationships used here are not based on observations  
171 from the present study's region of interest, the variation of a and b parameters yields an estimate of precipitation uncertainty.  
172 It is worth noting that a number of additional sources of radar measurement uncertainty exist that are not evaluated in depth  
173 here, including beam broadening, topographic blocking and scan elevation. However, this was not of primary concern since  
174 the goal of this study was to generate realistic spatial and temporal patterns of rainfall over the watershed with varying intensity  
175 that could be used to force the KINEROS2 hydrologic model. The goal was not to reproduce the observed hydrologic response  
176 resulting from a particular set of rainstorms.

177  
178 As a range of precipitation intensities for each storm result from the application of the five different Z-R relationships (e.g.,  
179 Figure S2 in Supplement), we utilize these as realistic storms of varying precipitation intensity to increase our storm sample  
180 size, such that we apply 34 storms \* 5 Z-R relations = 170 precipitation scenarios as inputs to KINEROS2. These 170 scenarios  
181 were then processed for ingestion into KINEROS2 (Figure. 2).

182

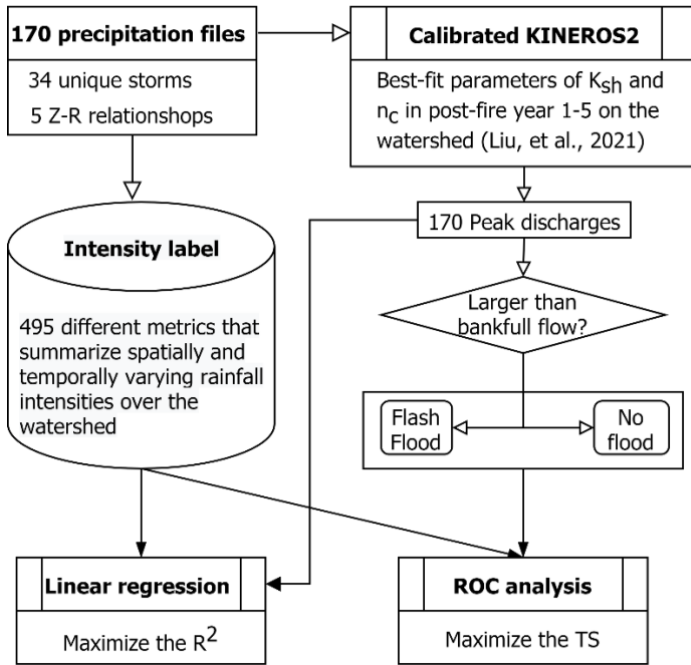


Figure 2: Delineation of rainfall intensity-duration threshold for post-fire flash flood

### 3.2 Summary metrics for spatially and temporally varying rainfall

In search of a spatiotemporal summary metric that may serve as a reliable flash flood threshold, we begin by describing a methodology to summarize spatially and temporally varying rainfall over a watershed. For a given rainstorm, the rainfall intensity time series at a single point, such as a single radar pixel, can be summarized by computing a moving average of intensity over a specified duration,  $D$ . Letting  $t$  denote time and  $R$  denote the cumulative rainfall (mm), we define the rainfall intensity over a duration  $D$  at any given pixel within the watershed as

$$I_D(t) = \frac{R(t) - R(t - D)}{D} \quad (1)$$

Here, we compute  $I_D(t)$  for each pixel for durations of 5, 10, 15, 30, and 60 minutes. Since the intensity in each radar pixel could have a unique value, we also need a way to summarize  $I_D(t)$  in space. One option would be to take the median of  $I_D(t)$  to determine a typical value of  $I_D$  within the watershed at each time,  $t$ . However, the median may not be a good predictor of flash flooding since one could envision a scenario where it is only raining over 1/3 of the watershed, yet it is raining with sufficient intensity to generate a flash flood. We therefore compute the  $j^{\text{th}}$  percentile of  $I_D(t)$  at each time,  $t$ , for  $j$  between 1 and 99. We denote the  $j^{\text{th}}$  percentile of  $I_D(t)$  as  $I_D^j(t)$ . For each rainstorm, we focus our analysis on the peak value of  $I_D^j(t)$



199 which we denote as  $I_D^j$ . As an example,  $I_{30}^{50}$  would be computed by defining  $I_{30}$  for all radar time steps within a rainstorm,  
200 determining the median value of  $I_{30}$  over the watershed at each of those time steps, and then taking the maximum of that time  
201 series of median  $I_{30}$  intensities. This analysis yields 495 different metrics ( $I_D^j$  for  $j=1,2,\dots,99$  and  $D=5,10,15,30,60$ ) that  
202 summarize spatially and temporally varying rainfall intensities over the watershed. In the following sections, we describe how  
203 we test the utility of each of these 495 different metrics as a flash flood threshold.

### 204 3.3 Hydrological modeling

205 We used the KINEROS2 (K2) hydrological model to simulate the rainfall partitioning, overland flow generation, and flood  
206 routing in the upper Arroyo Seco watershed. K2 is an event-scale, distributed-parameter, process-based watershed model,  
207 which has been used extensively for rainfall-runoff processes in semi-arid and arid watersheds (Smith et al., 1995; Goodrich  
208 et al., 2012). Liu et al (2021) used rain gage data in combination with the USGS stream gage installed at the outlet of the upper  
209 Arroyo Seco watershed to calibrate K2 during different stages of the post-fire recovery process. We use the same model setup  
210 for simulations in this study. In particular, the 41.5 km<sup>2</sup> watershed was discretized into 1289 hillslope planes and these planes  
211 were connected by a stream network of 519 channel segments based on a one-meter LiDAR-derived digital elevation model  
212 (DEM). After accounting for a fixed interception depth of 2.97 mm based on land cover look-up table in the Automated  
213 Geospatial Watershed Assessment toolkit (AGWA; Miller et al., 2007), infiltration of rainfall into soil is represented using the  
214 Parlange et al. (1982) approximation. Overland flow and channel flow are modeled by kinematic wave equations. Both  
215 saturated hydraulic conductivity on hillslopes ( $K_{sh}$ ) and hydraulic roughness in channels ( $n_c$ ) primarily determine runoff  
216 generation and the shape of hydrograph, including total runoff volume, peak discharge rate, time to peak (Canfield et al., 2005;  
217 Yatheendradas et al., 2008; Menberu et al., 2019). Other parameters, such as hydraulic roughness ( $n_h$ ) and capillary drive ( $G_h$ )  
218 on hillslopes, had a relatively minor impact on modelled runoff after the Station Fire in the upper Arroyo Seco watershed (Liu  
219 et al., 2021).

220  
221 **Table 1. Summary of model parameters for post-fire year 1, 2, 3, and 5. The saturated hydraulic conductivity on**  
222 **hillslopes ( $K_{sh}$ ) and hydraulic roughness in channels ( $n_c$ ) are the average of values calibrated in post-fire years 1, 2,**  
223 **3, and 5 (Liu et al., 2021)**

Post-fire Year	Calibration Events	$K_{sh}$ (mm/hr)	$n_c$ (s/[m <sup>1/3</sup> ])
1	12 Dec 2009	7.2	0.087
	17 Jan 2010		
	5 Feb 2010		
2	17 Dec 2010	13.8	0.275
	20 Mar 2011		



3	17 Mar 2012	18.5	0.320
	13 Apr 2012		
5	28 Feb 2014	23.8	0.280

Liu et al. (2021) found that both  $K_{sh}$  and  $n_c$  were lowest immediately after the fire.  $K_{sh}$  increased, on average, by approximately 4 mm/h/yr during the first five years of recovery, whereas  $n_c$  increased by more than a factor of two after 1 year of recovery and then remained relatively constant. We focus here on simulating the response to rainfall in the first five years following the fire where the watershed is likely most vulnerable to extreme responses. To represent the temporal changes in  $K_{sh}$  and  $n_c$  documented by Liu et al. (2021) following the fire, we used different values of  $K_{sh}$  and  $n_c$  for each post-fire year (i.e. post-fire years 1, 2, 3, and 5) based on the values calibrated by Liu et al. (2021) in post-fire years 1, 2, 3, and 5 (Table. 1). Liu et al. (2021) were unable to calibrate the necessary K2 parameters in post-fire year 4 so we do not perform any simulations to constrain flash flood thresholds in that year. Initial soil moisture is set to a volumetric soil-water content of 0.1, following Liu et al. (2021). Other parameters were also given the same values as the calibrated K2 model, including saturated hydraulic conductivity of channels (1 mm/hr), net capillary drive of channels (5 mm), hydraulic roughness of hillslopes ( $0.1 \text{ s}/(\text{m}^{1/3})$ ), net capillary drive of hillslopes (50 mm), and soil porosity of 0.4. With this model set-up, we simulate the response to each of the 170 rainstorms for post-fire years 1, 2, 3, and 5.

### 3.4 Rainfall intensity-duration thresholds

Each K2 simulation results in a modeled hydrograph at the watershed outlet. As a first step towards defining a flash flood threshold, it is necessary to determine, based on the modeled time series of discharge, whether or not a flash flood would have occurred. We defined the flash flood level as the discharge required to exceed bankfull flow (Sweeney, 1992), which we assumed was equal to the two-year flood (Leopold et al., 1964). To determine the discharge associated with the two-year flood, we performed a flood frequency analysis using HEC-SSP v2.2 (Bartles et al., 2019) based on annual maximum records at the USGS stream gage station (11098000). The discharge associated with the two-year flood at the stream gage station is  $15.3 \text{ m}^3/\text{s}$ , with a 95% confidence interval of  $12.3\text{-}19.2 \text{ m}^3/\text{s}$  (Figure S3). A flash flood threshold by this definition can be viewed as conservative since it may only indicate the onset of minor flooding as water begins to spill out of the channel. Based on this definition, we then used two approaches to identify the rainfall ID threshold for flash floods (Figure 2).

The first approach is based on a linear regression analysis that relates peak discharge with different rainfall ID metrics, namely  $I_D^j$  for different values of  $j$  and  $D$ . Using simulations of 170 rainfall-runoff events in each post-fire year, it is possible to determine a relationship for peak discharge ( $Q$ ) as a function of  $I_D^j$ . Then, the rainfall ID threshold can be found by determining

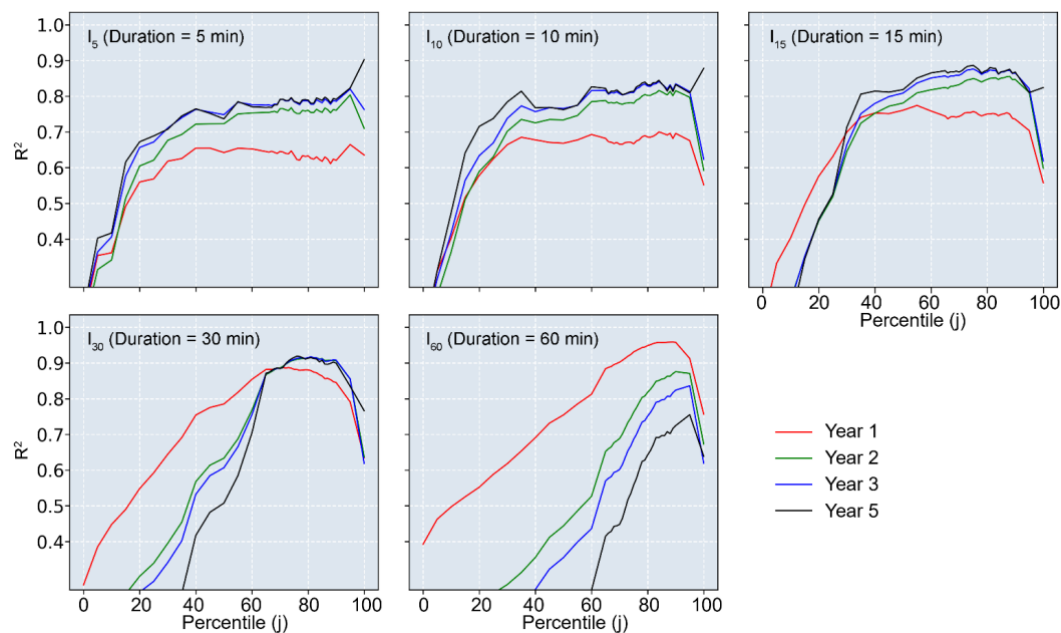


252 the rainfall intensity at which the peak discharge exceeds the bankfull capacity. The simplest quantitative relation is a linear  
 253 regression:

$$Q = mI_D^j + k \quad (2)$$

254 where  $Q$  is the peak discharge ( $\text{m}^3/\text{s}$ ) of a simulated hydrograph at the outlet,  $I_D^j$  denotes rainfall intensity ( $\text{mm}/\text{hr}$ ) for the  
 255 rainstorm that produced the hydrograph, and  $m$  and  $k$  denote the slope and y-intercept of the linear regression, respectively.  
 256

257  
 258 Considering the channel dimensions and resolution of the DEM used in the K2 model, we selected intensity-discharge ( $I_D^j - Q$ )  
 259 pairs associated with  $Q$  greater than  $2 \text{ m}^3/\text{s}$ . The parameters in the linear equation (1) with the maximum determination  
 260 coefficient ( $R^2_{\text{max}}$ ) were estimated using least-squares linear regression in the SciPy Python library for the selected  $I_D^j - Q$  pairs.  
 261 A total of 495 linear regressions were produced for each year because  $I_D^j$  can take on 495 different values (5 durations, 99  
 262 percentiles) for each rainstorm. For each post-fire year, we then identified the maximum  $R^2$  value for each duration as a  
 263 function of percentile from 1<sup>st</sup> to 99<sup>th</sup> (Figure 3). The rainfall ID threshold for flash flooding in each year was found, for each  
 264 duration, from the linear relation associated with the largest  $R^2$  (Figure 4).



265  
 266 **Figure 3: The determination coefficient ( $R^2$ ) associated with the linear regression between  $I_D^j$  and peak discharge in**  
 267 **post-fire year 1, 2, 3, and 5. Data used to fit the linear relation is from events with peak discharge greater than  $2 \text{ m}^3/\text{s}$ .**  
 268

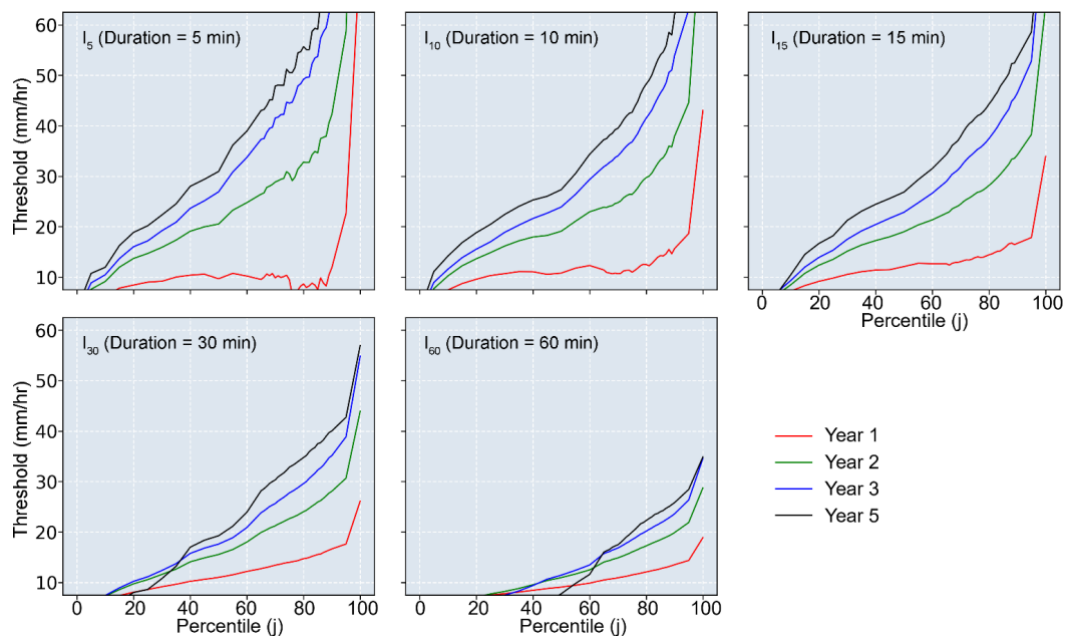


**Fig. 4 The rainfall intensity threshold for flash flood derived from the best linear relation for different durations and percentiles of the most intensive rainfall field in post-fire year 1, 2, 3, and 5.**

The second approach for determining rainfall ID thresholds is based on a receiver operating characteristic (ROC) analysis following Staley et al. (2013). We assess the utility of a potential threshold (e.g.  $I_{30}^{50} = 20\text{mm/hr}$ ), by computing the threat score (TS) associated with using that threshold to define the transition between rainstorms that produce flash floods and those that do not. The TS, as one of the ROC utility functions, measures the fraction of forecast events that were correctly predicted:

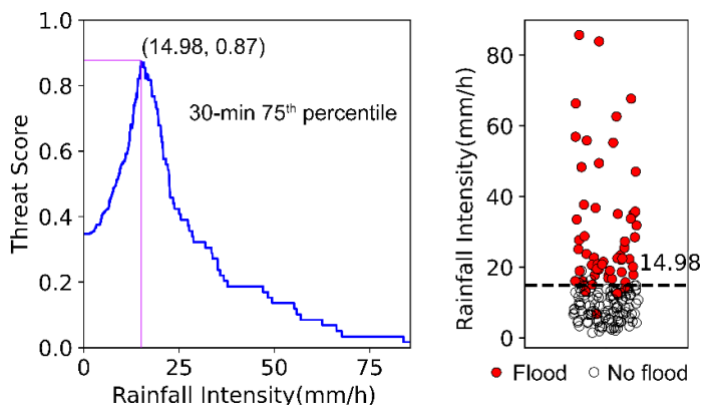
$$TS = \frac{TP}{TP + FP + FN} \quad (3)$$

where TP, FP, and FN denote a true positive, false positive, and false negative, respectively. Flash flood occurrence (true or false) is determined by comparing the peak discharge of each simulated hydrograph with the flash flood level ( $15.3 \text{ m}^3/\text{s}$ ). A TP represents an event where rainfall rates exceed the threshold (e.g.  $I_{30}^{50} = 20\text{mm/hr}$ ), and a flash flood occurred. A FP represents an event where rainfall rates exceed the threshold, but no flash flood occurred. FN events occur when rainfall rates were below the threshold, yet a flash flood occurred. The optimal TS is 1, meaning use of the threshold resulted in no false positives or false negatives.

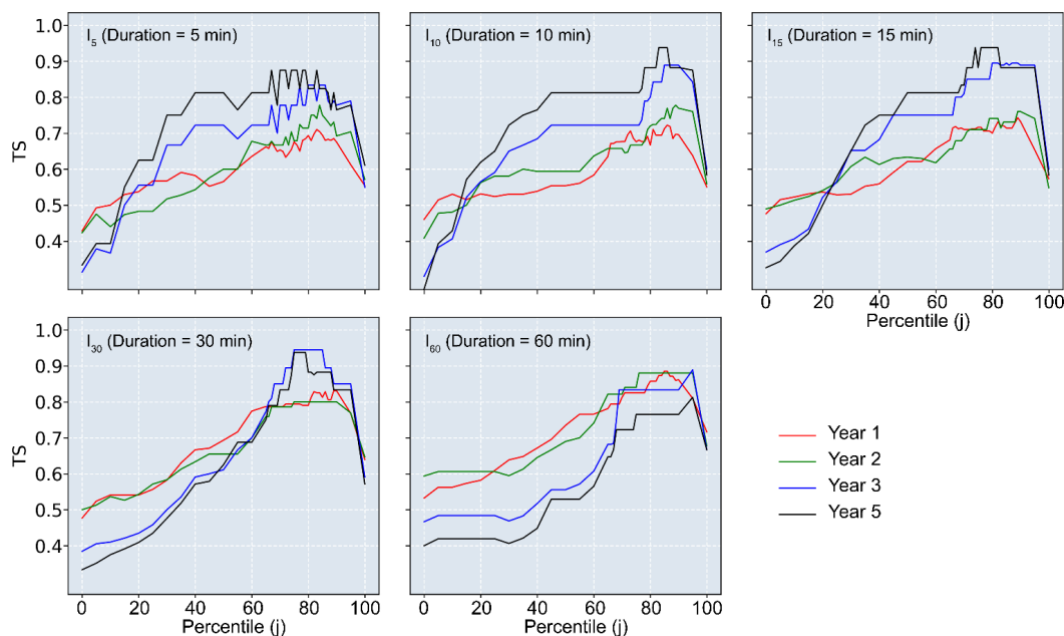
For a given rainfall intensity metric (e.g. the peak 75<sup>th</sup> percentile of  $I_{30}$ ,  $I_{30}^{75}$ , in year 1), we calculated TS for intensities ranging from 0-100 mm/hr at 0.01 mm/hr intervals (Figure 5). We then identified the threshold associated with the maximum TS



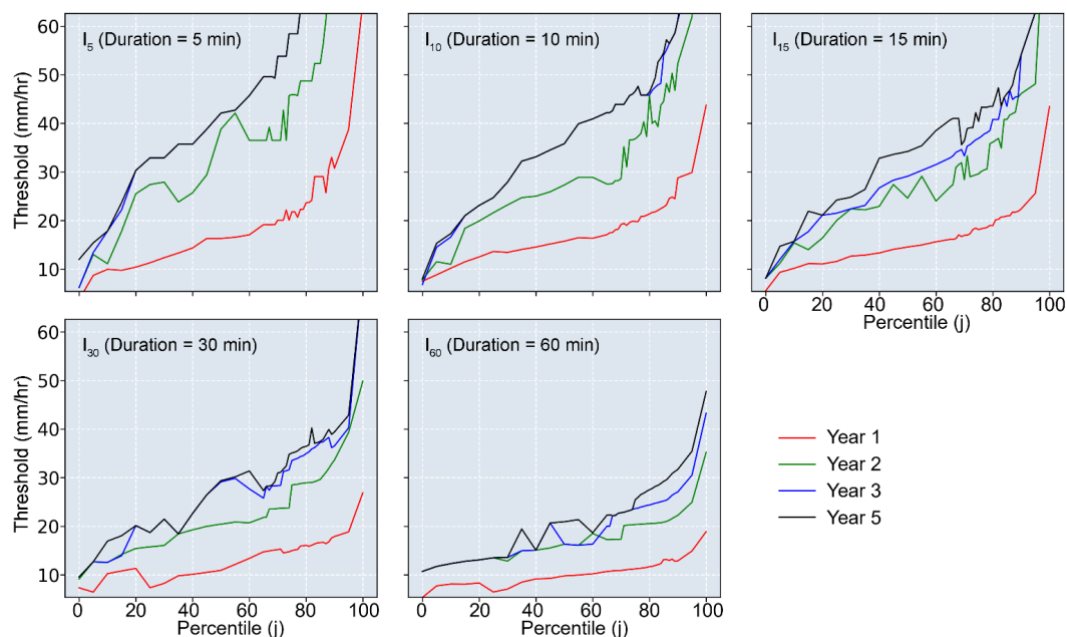
287 (TS<sub>max</sub>). The intensity associated with TS<sub>max</sub> is the optimal threshold for that rainfall metric (Figure 6). We determined the  
 288 optimal threshold associated with each of the 495 rainfall metrics for each post-fire year (1,2,3, and 5) (Figure 7).  
 289



290  
 291 **Fig. 5 Threat score (TS) of the peak 75<sup>th</sup> percentile of  $I_{30}$  in post-fire year 1. (a) Relationship between rainfall intensity**  
 292 **and TS; (b) Scatter plots of positive (flood, red circle) and negative (no flood, hollow circle) with the rainfall intensity**  
 293 **associated with the maximum TS.**



295  
 296 **Fig. 6 The threat scores (TS<sub>max</sub>) associated with flood occurrence and  $I_D^j$  in post-fire years 1, 2, 3, and 5. Data used to**  
 297 **analyze is from events with peak discharge greater than 2 m<sup>3</sup>/s.**  
 298



299  
 300 **Fig. 7** The rainfall intensity threshold for flash flood derived from the maximum of TS for different durations and  
 301 percentiles of the most intensive rainfall field in post-fire years 1, 2, 3, and 5.

302 **4 Results**

303 **4.1 Optimal summary metrics for defining rainfall ID thresholds**

304 Linear regression analyses suggest that there is a stronger relationship between  $I_D^j$  and peak discharge ( $Q$ ) as  $j$  increases, with  
 305 the exception of a rapid dropoff in  $R^2$  for  $j > 90$  and durations ( $D$ ) greater than 5 minutes (Figure 3). For durations of 5-15 min,  
 306  $R^2$  were low in the first 20-30 percentiles, then increased to 0.61-0.82 between the 30<sup>th</sup>-90<sup>th</sup> percentiles. Whereas the high  $R^2$   
 307 interval for durations of 30 min and 60 min were with the largest value between 0.92-0.96 between the 60<sup>th</sup>-90<sup>th</sup> percentiles in  
 308 year 1-5. The optimal rainfall threshold for flash floods (based on regressions of  $Q$  as a function of  $I_D^j$ ) increased from 13.3  
 309 mm/hr of  $I_{60}^{89}$  (the 89<sup>th</sup> percentile of 60 min peak rainfall field) in year 1 to 33.2 mm/hr of  $I_{30}^{76}$  (the 76<sup>th</sup> percentile of 30 min  
 310 peak rainfall field) in year 5 (Figure 4; Table 2). More generally, averaging rainfall intensity over a duration of 30 minutes and  
 311 choosing a percentile,  $j$ , of approximately 75-85 leads to threat scores of approximately 0.8 or greater for all post-fire years.  
 312 None of the other rainfall summary metrics performed this well across all post-fire years.

313  
 314 **Table. 2** The optimal metrics of rainfall ID and corresponding rainfall thresholds for flash floods in post-fire year 1-5

Linear regression	Receiver operating characteristic (ROC)
-------------------	---



Year	Rainfall metric	Equation	$R^2_{\max}$	Intensity (mm/hr)	Rainfall metric	$TS_{\max}$	Intensity (mm/hr)
1	$I_{60}^{89}$	$Q = 10.25 * I_{60}^{89} - 121.27$	0.958	13.3	$I_{60}^{85} - I_{60}^{86}$	0.89	13.1-13.2
2	$I_{30}^{81}$	$Q = 2.38 * I_{30}^{81} - 42.64$	0.916	24.4	$I_{60}^{76} - I_{60}^{95}$	0.88	20.4-25.0
3	$I_{30}^{81}$	$Q = 1.91 * I_{30}^{81} - 41.92$	0.917	30.0	$I_{30}^{75} - I_{30}^{85}$	0.94	33.5-37.3
5	$I_{30}^{76}$	$Q = 2.38 * I_{30}^{76} - 63.70$	0.919	33.2	$I_{30}^{75} - I_{30}^{79}$	0.94	35.1-36.3

315  
 316 Note: We denote the peak  $j^{\text{th}}$  percentile of  $I_D$  (rainfall intensity over a duration  $D$ ) as  $I_D^j$ . For example,  $I_{30}^{81}$  is the peak value of  
 317 the 81<sup>st</sup> percentile of  $I_{30}$  (rainfall intensity over 30-min).  
 318

319 Thresholds derived using the ROC method yielded broadly similar trends. The maximum threat score,  $TS_{\max}$ , generally  
 320 increased with  $j$  up to a point (approximately  $j=90$ ) and then began to decrease regardless of the choice of duration ( $D$ ) (Figure  
 321 6). The highest threat scores (TS), regardless of post-fire year or duration, were generally associated with the 60<sup>th</sup>-95<sup>th</sup>  
 322 percentiles. For events in years 1-2, the  $TS_{\max}$  (0.88-0.89) occurs around  $I_{60}^{85}$  (the 85<sup>th</sup> percentile of the peak  $I_{60}$  rainfall field);  
 323 for events in years 3-5, the  $TS_{\max}$  (0.94) occurs  $I_{30}^{75}-I_{30}^{79}$  (the 75<sup>th</sup>-79<sup>th</sup> percentile of the peak  $I_{30}$  rainfall field). The optimal  
 324 rainfall threshold for flash flood increased from 13.1 mm/hr of  $I_{60}^{85}-I_{60}^{86}$  (the 85<sup>th</sup>-86<sup>th</sup> percentile of 60 min peak rainfall field)  
 325 in year 1 to 36.3 mm/hr of  $I_{30}^{75}-I_{30}^{79}$  (the 75<sup>th</sup>-79<sup>th</sup> percentile of 30 min peak rainfall field) in year 5 (Table 2; Figure 6). As with  
 326 thresholds derived using the linear regression analysis, averaging rainfall intensity over a duration of 30 minutes and choosing  
 327 a percentile,  $j$ , of approximately 75-85 leads to threat scores of approximately 0.8 or greater for all post-fire years. Other  
 328 metrics did not perform this well, on average, across all post-fire years.

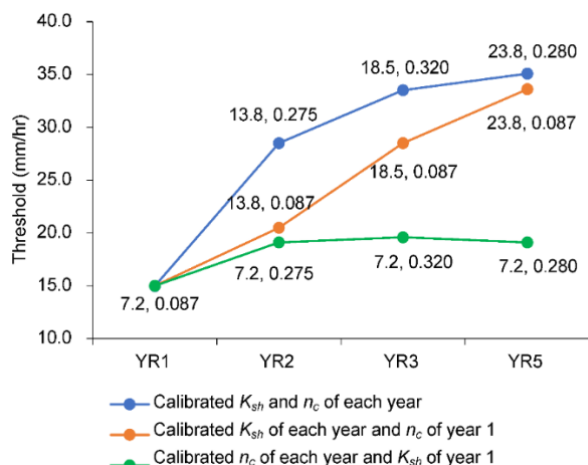
#### 329 4.2 Increases in rainfall intensity thresholds with time since fire

330 The rainfall intensity thresholds at each percentile significantly increased from post-fire year 1 to 5 (Figures 4 and 7). However,  
 331 the increase from year 1 to 2 is considerably larger than that from year 2 to 3 or from year 3 to year 5. Taking the  $I_{30}^{75}$  (the 75<sup>th</sup>  
 332 percentile of the peak  $I_{30}$  rainfall field) as an example due to its strong performance as a threshold for all post-fire years, the  
 333 thresholds based on linear regression analyses in year 1, 2, 3, and 5 are 14.0, 22.6, 27.8, and 32.9 mm/hr, respectively; the  
 334 ROC-based  $I_{30}^{75}$  thresholds in year 1, 2, 3, and 5 are 15.0, 28.5, 33.5, and 35.0 mm/hr, respectively (Figure 7).  
 335

336 We are also able to use the model to assess the individual impacts of temporal changes in  $K_{sh}$  and  $n_c$  on temporal variations in  
 337 the flash flood threshold. If  $K_{sh}$  is allowed to vary from year to year (Table 1) and  $n_c$  is held fixed at its calibrated value for  
 338 year 1, then ROC analysis indicates that the optimal threshold of  $I_{30}^{75}$  still increases with time since burning (Figure 8).



339 However, it increases slower than the case where both  $K_{sh}$  and  $n_c$  are allowed to vary with time (Figure 8). If  $n_c$  is allowed to  
340 vary from year to year (Table 1) and  $K_{sh}$  is held fixed at its calibrated value for year 1, then ROC analysis indicates that the  
341 optimal threshold associated with  $I_{30}^{75}$  increases from year 1 to year 2 but then stays roughly constant as time increases (Figure  
342 8). Therefore, changes in  $K_{sh}$  and  $n_c$  both play important roles in determining the degree to which the flash flood threshold  
343 increases from year 1 to year 2, but that further increases in the threshold in years three and five are driven mainly by increases  
344 in  $K_{sh}$  as a function of time since burning.



345 **Figure 8: The ROC (receiver operating characteristic) based thresholds for  $I_{30}^{75}$  in each year with different model**  
346 **settings. Pairs of  $K_{sh}$  (saturated hydraulic conductivity on hillslopes) and  $n_c$  (Manning's  $n$  in channels) in each model**  
347 **are along with the data points.**  
348

## 349 5 Discussion

### 350 5.1 Implication of optimal metrics of rainfall intensity for flood warning

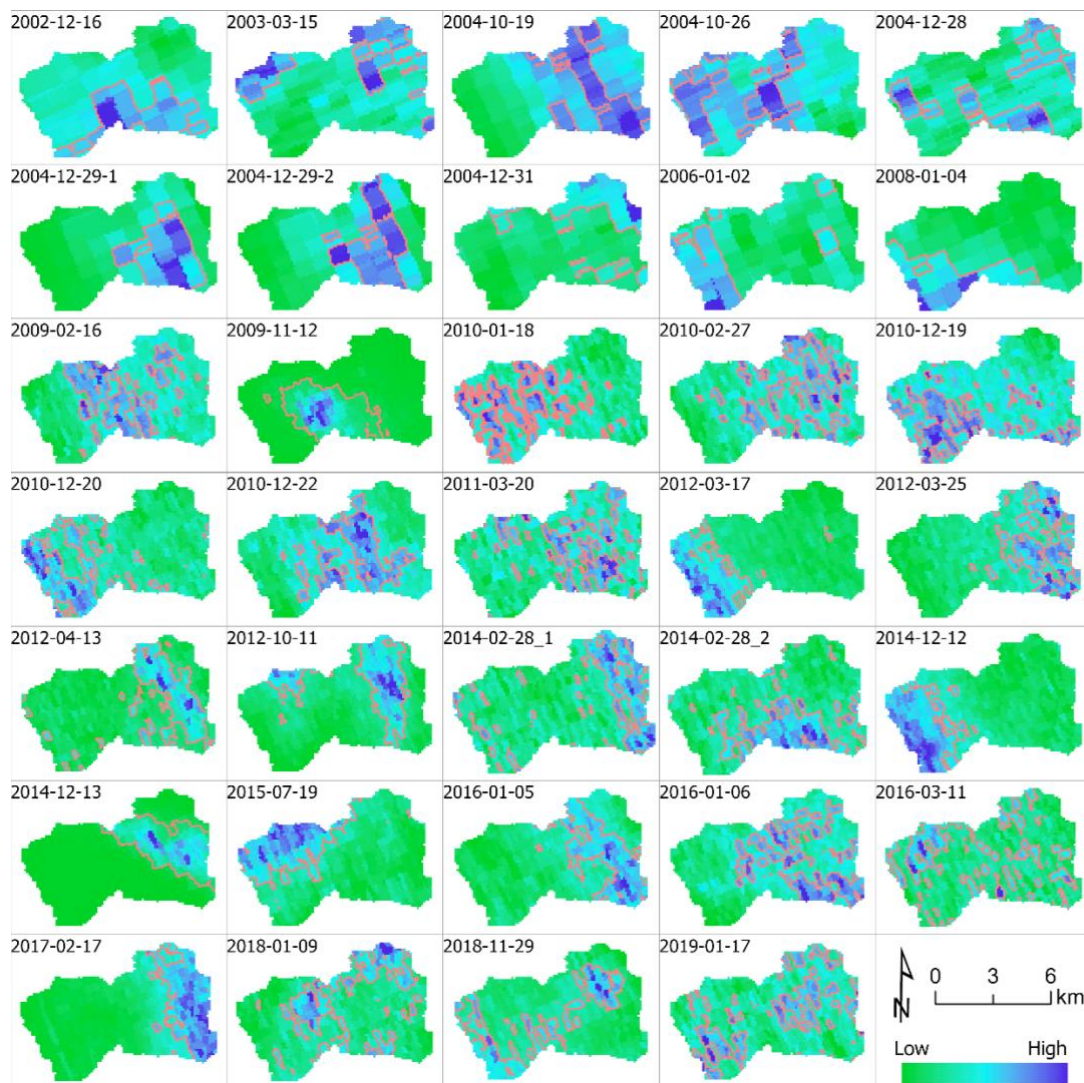
351 Rain gage records, which provide rainfall intensity data at a single point, are often used to define rainfall ID thresholds in  
352 debris-flow and flash flood studies (e.g. Moody and Martin, 2001; Cannon et al. 2008; Cannon et al. 2011; Guzzetti et al.  
353 2008; Kean et al., 2011; Staley et al., 2013; Raymond et al., 2020; McGuire and Youberg, 2020). Using point source data to  
354 define thresholds for debris flows and flash floods is ideal when rainfall intensity does not vary substantially over the  
355 watershed, an assumption that is most appropriate for watershed areas less than several square kilometers. Radar-derived  
356 rainfall data has the advantage of providing spatially explicit information over an entire watershed at a high-temporal resolution  
357 (e.g. 5 minute). However, one challenge in using radar-derived precipitation to define thresholds is the need to condense  
358 spatially and temporally variable rainfall intensity information down to a single rainfall intensity metric. Regardless of whether  
359 the approach to determining an ID threshold involves fitting empirical relationships (e.g., Moody and Martin, 2001; Cannon



360 et al., 2008) or using ROC analysis (e.g., Staley et al., 2013), a single metric is required to represent the rainfall intensity for  
361 each duration.

362  
363 We summarized spatially variable rainfall intensity data over the watershed by computing the peak value of  $I_D^j(t)$ , the  $j^{\text{th}}$   
364 percentile of  $I_D(t)$  for each rainstorm. We used two different techniques, one based on a linear regression analysis and one  
365 based on ROC analysis (Figure 2), to define thresholds for flash floods in post-fire years 1, 2, 3, and 5. Although the optimal  
366 metrics produced by the two approaches are not identical, they are generally similar in each post-fire year. In particular, high  
367  $R^2$  and  $TS_{\text{max}}$  values are associated with metrics of the peak 75<sup>th</sup>-85<sup>th</sup> percentile of rainfall intensity averaged over 30-60 minutes  
368 ( $I_D^j$  for  $75 \leq j \leq 85, D = 30, 60$ ). In other words, a good indicator of the potential for a flash flood is the presence of intense  
369 pulses of rainfall over durations of 30-60 minutes that cover at least 15%-25% of the watershed (Figure 9). This finding  
370 highlights the ability of rainstorms to produce flash floods even if they don't cover the majority of the watershed with intense  
371 rainfall. If rainfall over the majority of the watershed was required to produce flash floods, then we would expect that  $I_D^j$  with  
372  $j < 50$  would be a better predictor of flash floods. Previous work has also identified that 30-minute rainfall intensity works well  
373 for predicting flash floods and debris flows (Moody and Martin, 2001; Kean et al., 2011; Staley et al., 2013). The finding that  
374  $I_{30}^j$  and  $I_{60}^j$  work best as thresholds when  $75 \leq j \leq 85$  could be helpful when issuing flash flood warnings based on radar-  
375 derived precipitation estimates or data from several real-time rain gages within a watershed. Current operational forecast  
376 models such as the High Resolution Rapid Refresh model have a horizontal resolution of 3km and minimum temporal  
377 resolution of 15 minutes (Benjamin et al. 2016; NOAA 2021a), such that it is feasible to use  $I_{30}^j$  and  $I_{60}^j$  in an operational  
378 forecast setting. Where sufficient operational NEXRAD weather radar coverage is present, radar-derived precipitation  
379 estimates such as the MRMS (Zhang et al. 2016) can provide near-real-time precipitation estimates at 1 km and as fine as 15  
380 min temporal resolution (NOAA 2021b). In the case of poor radar coverage, gap-filling radars may be temporarily deployed  
381 or installed (e.g., Jorgensen et al. 2011; Cifelli et al. 2018) to provide information necessary for accurate precipitation estimates.  
382 While the magnitude of rainfall thresholds estimated here may only work for similar, recently burned watersheds within the  
383 San Gabriel Mountains, the use of metrics such as  $I_{30}^{75}$  as a reliable predictor of post-fire flash floods may be more general.  
384 Further testing is needed in watersheds with different watershed size, topographic characteristics, landscape, and burn severity  
385 patterns.

386



387  
 388 **Figure 9: Snapshots of the spatial patterns of  $I_{30}^{75}$  of 34 unique storms. The peak  $j^{\text{th}}$  percentile of  $I_D$  (rainfall intensity**  
 389 **over a duration  $D$ ) is denoted as  $I_D^j$ .  $I_{30}^{75}$  is the peak value of the 75<sup>st</sup> percentile of  $I_{30}$  (rainfall intensity over 30-min).**  
 390 **Red contours delineate the pixels with rainfall intensities larger than  $I_{30}^{75}$  of each storm.**

391  
 392 Several limitations are present in this work. First, we assess a small number of storm events (34) in the area as we are limited  
 393 by the length of radar and gage records as well as and the number of events that impact the indicator rain gages. However, the  
 394 advantage of using observed storms rather than using a rainfall generator (e.g., Zhao et al., 2019; Evin et al., 2018) is that our  
 395 results represent spatial and temporal precipitation patterns that are physically realistic. Second, the challenges of radar  
 396 observations and application of Z-R relationships to convert reflectivity to precipitation also presents challenges in accurately  
 397 representing precipitation values. This can be addressed in future work through studies to constrain Z-R relationships for

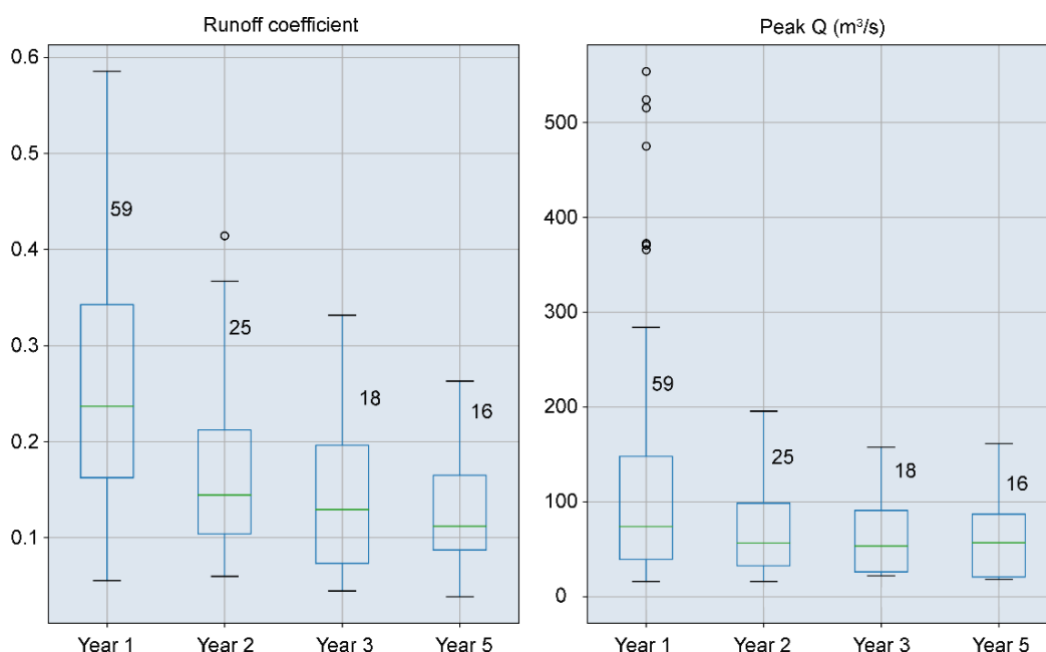


398 storms producing intense rainfall in this region and through the deployment or installation of high-resolution gap-filling radars  
399 (e.g., Johnson et al. 2019).

## 400 5.2 Increasing rainfall intensity thresholds with time since fire

401 In this study we employed the K2 model calibrated by Liu et al. (2021) to parameterize hydrologic changes affecting Hortonian  
402 overland flow within a five-year period following fire. Hillslope saturated hydraulic conductivity ( $K_{sh} = 7.2$  mm/hr) and  
403 hydraulic roughness in channels ( $n_c = 0.087$  s/m<sup>1/3</sup>) were lowest immediately after fire (Table 1), resulting in high runoff  
404 coefficients and low rainfall thresholds in post-fire year 1. In later years, with  $K_{sh}$  and  $n_c$  gradually increasing (Table 1), more  
405 rainfall infiltrated into soil and there was increased attenuation of flood peaks. Simulations indicate that the number of flash-  
406 flood-producing rainstorms decreased from 59 in year 1 to 25, 18, and 16 in years 2, 3, and 5, respectively. Runoff coefficients  
407 and peak discharge of simulated hydrographs also decreased with time since fire (Figure 10). Given the same precipitation  
408 ensemble, the likelihood of flash floods significantly decreased with time. The peak discharge produced by the highest intensity  
409 rainfall event with  $I_{60}^{75}$  of 51.8 mm/hr was 554.0 m<sup>3</sup>/s in the first year after the fire, which is three times greater than the peak  
410 discharges of 157.5 m<sup>3</sup>/s in year 3 and 161.2 m<sup>3</sup>/s in year 5 produced by the same rainstorm. From a flood hazard perspective,  
411 the downstream area may be exposed to a 1000-year flood under the recently burned condition (less than one year since the  
412 fire), whereas the discharge produced in years three and five would amount to roughly a 30- to 40-year flood (Figure S3).

413



414

415 **Figure 10: Box plots showing the runoff coefficient and peak discharge of flash floods in post-fire year 1, 2, 3, and 5.**

416 **The numbers of flash floods in each year are displayed next to the box.**



417 We were also able to perform numerical experiments to quantify the relative importance of temporal changes in  $K_{sh}$  and  $n_c$  on  
418 temporal variations in the flash flood threshold (Figure 8). Results suggest that changes in vegetation and grain roughness,  
419 which are likely to influence  $n_c$ , throughout the recovery process are less important for determining flash flood potential in our  
420 study area relative to changes to saturated hydraulic conductivity on hillslopes. It is worth noting that temporal changes in  
421 other model parameters (e.g., hydraulic roughness on hillslopes, capillary drive) may play more of a role in driving changes  
422 in post-fire flash flood thresholds in other settings. In this study, however, we focus on changes in  $K_{sh}$  and  $n_c$  because Liu et  
423 al. (2021) were able to detect temporal changes in  $n_c$  and  $K_{sh}$  through time and unable to detect similar temporal changes in  
424 other hydrologic parameters (e.g., hydraulic roughness on hillslopes, capillary drive) due to their relatively minor influence on  
425 runoff in the study watershed.

426  
427 In this study, the optimal flash flood thresholds increased from  $I_{30}^{75} = 14.0\text{-}15.0$  mm/hr in post-fire year 1, to 22.6-28.5 mm/hr  
428 in year 2, and 22.9-35.1 mm/hr in post-fire year 5 (Figure 4 and 7; Table 2). In the San Gabriel Mountains and nearby San  
429 Bernardino and San Jacinto Mountains, Cannon et al. (2008) estimated rainfall thresholds of  $I_{30}=9.5$  mm/hr and for flash floods  
430 and debris flows in the first winter rainy season following fire. They found that the thresholds for flash floods and debris flows  
431 increased to  $I_{30}=19.8$  mm/hr in post-fire year 2. The thresholds that we infer from hydrological modeling are greater than those  
432 reported by Cannon et al. (2008), which may be partly due to differences in (1) data and methods used and (2) the size of the  
433 studied watersheds. Our results are driven by a hydrologic model, forced with a radar precipitation ensemble that consists of  
434 170 rainstorms that contain a variety of storm types that impact southern California. The occurrence of a flash flood is based  
435 on exceedance of the maximum channel capacity and we summarize temporal changes in the rainfall ID threshold using  $I_{30}^{75}$   
436 since we find this to be a reliable metric for all post-fire years included in this study. In contrast, Cannon et al. (2008)  
437 established rainfall ID relations by using observations of rainstorms and hydrological response in the two years following fire  
438 in 87 small watersheds (0.2-4.6 km<sup>2</sup>). They base their thresholds on rainfall characteristics that produced either flash floods or  
439 debris flows whereas we focus solely on flash floods. In their dataset, flash floods and debris flows were identified by  
440 investigating flood and debris flow deposits at the outlet of those small watersheds in the field. Despite differences in the  
441 magnitude of the thresholds, the increase in the threshold from post-fire year 1 to year 2 in both studies are quite close. This  
442 agreement provides support for the use of simulation-based approaches to inform temporal shifts in rainfall ID thresholds.

443  
444 During the recovery process, increasing thresholds for flash floods and debris flows have also been identified in other areas at  
445 different scales by either observation- or simulation-based studies, such as hillslopes in the Colorado Front Range (Ebel, 2020)  
446 and small watersheds in Australia (Noske et al., 2016). The consistent increase in rainfall ID thresholds with time since fire in  
447 different geographic and ecological zones implies that hydraulic and hydrologic models may be useful tools for exploring how  
448 transient effects of fire translate into changes in water-related hazards. Particularly when historic data is limited and traditional  
449 empirical methods are impractical for defining thresholds, the role of hydraulic and hydrological models becomes more  
450 important.



## 451 **6 Conclusions**

452 We used 250 m, 5-minute radar-derived precipitation estimates over a 41.5 km<sup>2</sup> watershed in combination with a calibrated  
453 hydrological model to estimate the rainfall intensity thresholds for post-fire flash floods as a function of time since burning.  
454 The optimal threshold for predicting the occurrence of a flash flood in our study areas is the 75<sup>th</sup>-85<sup>th</sup> percentile of peak rainfall  
455 intensity averaged over 30-60 minutes, i.e.,  $I_{30}^{75}$ - $I_{30}^{85}$ . In other words, a flash flood tends to be produced when rainfall intensity  
456 over 15%-25% of the watershed area exceeds a critical value. A threshold based on  $I_{30}^{75}$  performs consistently well for post-  
457 fire years 1, 2, 3, and 5, although the magnitude of the threshold increases with time since burning. For the watershed studied,  
458 the  $I_{30}^{75}$  threshold increases from 14.0-15.0 mm/hr for year 1 to 22.6-28.5 mm/hr, 27.8-33.5 mm/hr, and 32.9-35.1 mm/hr, for  
459 years 2, 3, and 5 respectively. Increases in the threshold value of  $I_{30}^{75}$  can be primarily attributed to increases in  $K_{sh}$  rather than  
460  $n_c$  during the hydrological recovery process. The increase in the magnitude of the threshold from year 1 to year 2 is consistent  
461 with previous observations from nearby areas in southern California. Results provide a methodology for using radar-derived  
462 precipitation estimates and hydrological modeling to estimate flash flood thresholds for improved warning and mitigation of  
463 post-fire hydrologic hazards. Thresholds developed through these methods can then be built into operational tools that use  
464 incoming radar data to evaluate flash flood hazard in near-real time or precipitation forecasts to evaluate potential for flash  
465 flood hazard in burned watersheds.

## 466 **Author contributions**

467 TL and LM conceived the study. TL, LM, NO and FC contributed to the development and design of the methodology. TL  
468 analysed and prepared the manuscript with review and analysis contributions from LM, NO and FC.

## 469 **Competing interests**

470 The authors declare that they have no conflict of interest.

## 471 **Acknowledgments:**

472 Haiyan Wei, Carl L. Unkrich, and David C. Goodrich, who are from the KINEROS2 development group in the USDA ARS  
473 Southwest Watershed Research Center in Tucson, helped with the setting up of the KINEROS2 model and ingestion of the  
474 RADAR precipitation data into the model. We are thankful for their great help.



475 **Financial support**

476 This work was supported by the National Oceanic and Atmospheric Administration (NOAA) Collaborative Science,  
477 Technology, and Applied Research (CSTAR) Program under grant NA19NWS4680004 and by the National Integrated  
478 Drought Information System (NIDIS) through Task Order 1332KP20FNRMT0012.

479 **References**

- 480 Bartles, M., Brunner, G., Fleming, M., Faber, B., Karlovits, G., and Slaughter, J.: HEC-SSP Statistical Software Package  
481 Version 2.2, June 2019.
- 482 Benjamin, S. G., Weygandt, S. S., Brown, J. M., Hu, M., Alexander, C. R., Smirnova, T. G., Olson, J. B., James, E. P., Dowell,  
483 D. C., Grell, G. A., Lin, H., Peckham, S. E., Smith, T. L., Moninger, W. R., Kenyon, J. S., & Manikin, G. S. (2016). A North  
484 American Hourly Assimilation and Model Forecast Cycle: The Rapid Refresh, *Monthly Weather Review*, 144(4), 1669-1694.  
485 Retrieved May 23, 2021, from <https://journals.ametsoc.org/view/journals/mwre/144/4/mwr-d-15-0242.1.xml>
- 486 Canfield, H. E., Goodrich, D. C., & Burns, I. S. (2005). Selection of parameters values to model post-fire runoff and sediment  
487 transport at the watershed scale in southwestern forests. *Proceedings of the 2005 Watershed Management Conference -*  
488 *Managing Watersheds for Human and Natural Impacts: Engineering, Ecological, and Economic Challenges*, 40763(June  
489 2015), 561–572. [https://doi.org/10.1061/40763\(178\)48](https://doi.org/10.1061/40763(178)48)
- 490 Cannon, F., and Coauthors, 2020: Observations and Predictability of a High-Impact Narrow Cold-Frontal Rainband over  
491 Southern California on 2 February 2019. *Wea. Forecasting*, 35, 2083–2097, <https://doi.org/10.1175/WAF-D-20-0012.1>.
- 492 Cannon, S. H., Boldt, E. M., Laber, J. L., Kean, J. W., & Staley, D. M. (2011). Rainfall intensity-duration thresholds for  
493 postfire debris-flow emergency-response planning. *Natural Hazards*, 59(1), 209–236. [https://doi.org/10.1007/s11069-011-](https://doi.org/10.1007/s11069-011-9747-2)  
494 [9747-2](https://doi.org/10.1007/s11069-011-9747-2)
- 495 Cannon, S. H., Gartner, J. E., Wilson, R. C., Bowers, J. C., & Laber, J. L. (2008). Storm rainfall conditions for floods and  
496 debris flows from recently burned areas in southwestern Colorado and southern California. *Geomorphology*, 96, 250–269.  
497 <https://doi.org/10.1016/j.geomorph.2007.03.019>
- 498 Carsel, R. F., & Parrish, R. S. (1988). Developing joint probability distributions of soil water retention characteristics. *Water*  
499 *Resources Research*, 24(5), 755–769. <https://doi.org/10.1029/WR024i005p00755>
- 500 Cifelli, R., Chandrasekar, V., Chen, H., & Johnson, L. E. (2018). High resolution radar quantitative precipitation estimation in  
501 the San Francisco Bay Area: Rainfall monitoring for the urban environment. *Journal of the Meteorological Society of Japan*.  
502 *Ser. II*, 96, 141-155.
- 503 Dyrness, C. (1976), Effect of Wildfire on Soil Wettability in the High Cascades of Oregon, U.S. Dept. of Agriculture, Forest  
504 Service, Pacific Northwest forest and Range Experiment Station, Portland, Oreg.



- 505 Ebel, B. A. (2020). Temporal evolution of measured and simulated infiltration following wildfire in the Colorado Front Range,  
506 USA: Shifting thresholds of runoff generation and hydrologic hazards. *Journal of Hydrology*, 585(March), 124765.  
507 <https://doi.org/10.1016/j.jhydrol.2020.124765>
- 508 Ebel, B. A., & Martin, D. A. (2017). Meta - analysis of field - saturated hydraulic conductivity recovery following wildland  
509 fire : Applications for hydrologic model parameterization and resilience assessment. *Hydrological Processes*. 2017; 31: 3682–  
510 3696. <https://doi.org/10.1002/hyp.11288>
- 511 Ebel, B. A., & Moody, J. A. (2013). Rethinking infiltration in wildfire-affected soils. *Hydrological Processes*, 27(10), 1510–  
512 1514. <https://doi.org/10.1002/hyp.9696>
- 513 Ebel, B. A., & Moody, J. A. (2017). Synthesis of soil-hydraulic properties and infiltration timescales in wildfire-affected soils.  
514 *Hydrological Processes*, 31(2), 324–340. <https://doi.org/10.1002/hyp.10998>
- 515 Evin, G., Favre, A.-C., & Hingray, B. (2018). Stochastic generation of multi-site daily precipitation focusing on extreme  
516 events, *Hydrol. Earth Syst. Sci.*, 22, 655–672, <https://doi.org/10.5194/hess-22-655-2018>.
- 517 Gillett NP, Weaver AJ, Zwiers FW, Flannigan MD. (2004). Detecting the effect of climate change on Canadian forest fires.  
518 *Geophysical Research Letters* 31. <https://doi-org.ezproxy2.library.arizona.edu/10.1029/2004>
- 519 Goodrich, D. C., Burns, I. S., Unkrich, C. L., Semmens, D. J., Guertin, D. P., Hernandez, M. (2012). KINEROS2/AGWA:  
520 Model use, Calibration, and Validation. *Transactions of the ASABE*, 55(4), 1561–1574. <https://doi.org/10.13031/2013.42264>
- 521 Guzzetti, F., Peruccacci, S., Rossi, M., & Stark, C. P. (2008). The rainfall intensity-duration control of shallow landslides and  
522 debris flows: An update. *Landslides*, 5(1), 3–17. <https://doi.org/10.1007/s10346-007-0112-1>
- 523 Hubbert, K. R., & Oriol, V. (2005). Temporal fluctuations in soil water repellency following wildfire in chaparral steeplands,  
524 southern California. *International Journal of Wildland Fire*, 14(4), 439–447. <https://doi.org/10.1071/WF05036>
- 525 Hubbert, K. R., Wohlgemuth, P. M., & Beyers, J. L. (2012). Effects of hydromulch on post-fire erosion and plant recovery in  
526 chaparral shrublands of southern California. *International Journal of Wildland Fire*, 21(2), 155–167.  
527 <https://doi.org/10.1071/WF10050>
- 528 Huffman, E. L., MacDonald, L. H., & Stednick, J. D. (2001). Strength and persistence of fire-induced soil hydrophobicity  
529 under ponderosa and lodgepole pine, Colorado Front Range. *Hydrological Processes*, 15(15), 2877–2892.  
530 <https://doi.org/10.1002/hyp.379>
- 531 Johnson, LE, Cifelli, R, White, A. Benefits of an advanced quantitative precipitation information system. *J Flood Risk*  
532 *Management*. 2020; 13 ( Suppl. 1):e12573. <https://doi.org/10.1111/jfr3.12573>
- 533 Jorgensen, D. P., Hanshaw, M. N., Schmidt, K. M., Laber, J. L., Staley, D. M., Kean, J. W., & Restrepo, P. J. (2011). Value  
534 of a dual-polarized gap-filling radar in support of southern California post-fire debris-flow warnings. *Journal of*  
535 *Hydrometeorology*, 12(6), 1581-1595.



- 536 Kean, J. W., Staley, D. M., & Cannon, S. H. (2011). In situ measurements of post-fire debris flows in southern California:  
537 Comparisons of the timing and magnitude of 24 debris-flow events with rainfall and soil moisture conditions. *Journal of*  
538 *Geophysical Research: Earth Surface*, 116(4), 1–21. <https://doi.org/10.1029/2011JF002005>
- 539 Kean, J. W., Staley, D. M., & Cannon, S. H. (2011). In situ measurements of post-fire debris flows in southern California:  
540 Comparisons of the timing and magnitude of 24 debris-flow events with rainfall and soil moisture conditions. *Journal of*  
541 *Geophysical Research: Earth Surface*, 116(4), 1–21. <https://doi.org/10.1029/2011JF002005>
- 542 Kitzberger, T., Falk, D. A., Westerling, A. L., & Swetnam, T. W. (2017). Direct and indirect climate controls predict  
543 heterogeneous early-mid 21st century wildfire burned area across western and boreal North America. *PLoS ONE*, 12(12), 1–  
544 24. <https://doi.org/10.1371/journal.pone.0188486>
- 545 Lamb, M. P., Scheingross, J. S., Amidon, W. H., Swanson, E., & Limaye, A. (2011). A model for fire-induced sediment yield  
546 by dry ravel in steep landscapes. *Journal of Geophysical Research: Earth Surface*, 116(3), 1–13.  
547 <https://doi.org/10.1029/2010JF001878>
- 548 Larsen, I. J., MacDonald, L. H., Brown, E., Rough, D., Welsh, M. J., Pietraszek, J. H., et al. (2009). Causes of post-fire runoff  
549 and erosion: Water repellency, cover, or soil sealing? *Soil Science Society of America Journal*, 73(4), 1393–1407.  
550 <https://doi.org/10.2136/sssaj2007.0432>
- 551 Leopold, L.B., Wolman, M.G., and Miller, J.P. 1964. *Fluvial Processes in Geomorphology*. Dover, New York.
- 552 Liu, T., McGuire, L. A., Wei, H. Y., Renger, F. K., Gupta, H., Ji, L., Goodrich, D. C. (2021). The timing and magnitude of  
553 changes to Hortonian overland flow at the watershed scale during the post-fire recovery process. *Hydrological Processes*.  
554 35(5). <https://doi.org/10.1002/hyp.14208>
- 555 Marshall, J. S., and W. M. K. Palmer, 1948: THE DISTRIBUTION OF RAINDROPS WITH  
556 SIZE. *J. Meteor.*, 5, 165–166, [https://doi.org/10.1175/1520-0469\(1948\)005<0165:TDORWS>2.0.CO;2](https://doi.org/10.1175/1520-0469(1948)005<0165:TDORWS>2.0.CO;2).
- 557 McGuire, L. A., & Youberg, A. M. (2020). What drives spatial variability in rainfall intensity-duration thresholds for post-  
558 wildfire debris flows? Insights from the 2018 Buzzard Fire, NM, USA. *Landslides*, December 2019.  
559 <https://doi.org/10.1007/s10346-020-01470-y>
- 560 Meles, M. B., Goodrich, D. C., Gupta, H. V., Burns, S. I., Unkrich, C. L., Razavi, S., Guertin, D. P. (2019). Uncertainty and  
561 parameter sensitivity of the KINEROS2 physically-based distributed sediment and runoff model. In *Federal Interagency*  
562 *Sedimentation and Hydrologic Modeling Conference*.
- 563 Miller, S. N., Semmens, D. J., Goodrich, D. C., Hernandez, M., Miller, R. C., Kepner, W. G., & Guertin, D. P. (2007). The  
564 automated geospatial watershed assessment tool. *851 Environmental Modelling and Software*. 22(3), 365-377. 852  
565 <https://doi.org/10.1016/j.envsoft.2005.12.004>
- 566 Moody, J. A., & Ebel, B. A. (2012). Hyper-dry conditions provide new insights into the cause of extreme floods after wildfire.  
567 *Catena*, 93, 58–63. <https://doi.org/10.1016/J.CATENA.2012.01.006>
- 568 Moody, J. A., & Martin, D. A. (2001). Post-fire, rainfall intensity – peak discharge relations for three mountainous watersheds  
569 in the western USA. 2993(July), 2981–2993. <https://doi.org/10.1002/hyp.386>



- 570 Moreno, H. A., Gourley, J. J., Pham, T. G., & Spade, D. M. (2020). Utility of satellite-derived burn severity to study short-  
571 and long-term effects of wildfire on streamflow at the basin scale. *Journal of Hydrology*, 580(October 2019), 124244.  
572 <https://doi.org/10.1016/j.jhydrol.2019.124244>
- 573 NOAA National Weather Service (NWS) Radar Operations Center (1991): NOAA Next Generation Radar (NEXRAD) Level  
574 2 Base Data. NOAA National Centers for Environmental Information. doi:10.7289/V5W9574V
- 575 NOAA. (2021a). High-Resolution Rapid Refresh (HRRR) Model [Dataset]. <https://registry.opendata.aws/noaa-hrrr-pds/>
- 576 NOAA. (2021b) Multi-Radar/Multi-Sensor System (MRMS). [Dataset]. <https://www.nssl.noaa.gov/projects/mrms/>
- 577 Noske, P. J., Nyman, P., Lane, P. N. J., & Sheridan, G. J. (2016). Effects of aridity in controlling the magnitude of runoff and  
578 erosion after wildfire. *Water Resources Research*, 52(6), 4338–4357. <https://doi.org/10.1002/2015WR017611>
- 579 Oakley, N. S., Lancaster, J. T., Kaplan, M. L., & Ralph, F. M. (2017). Synoptic conditions associated with cool season post-  
580 fire debris flows in the Transverse Ranges of southern California. *Natural Hazards*, 88(1), 327–354.  
581 <https://doi.org/10.1007/s11069-017-2867-6>
- 582 Oakley, N. S., J. T. Lancaster, B. J. Hatchett, J. Stock, F. M. Ralph, S. Roj, & S. Lukashov. (2018a). A 22-Year climatology  
583 of cool season hourly precipitation thresholds conducive to shallow landslides in California. *Earth Interact.*, 22, 1–35,  
584 <https://doi.org/10.1175/EI-D-17-0029.1>.
- 585 Oakley, N. S., Cannon, F., Munroe, R., Lancaster, J. T., Gomberg, D., & Ralph, F. M. (2018b). Brief communication:  
586 Meteorological and climatological conditions associated with the 9 January 2018 post-fire debris flows in Montecito and  
587 Carpinteria, California, USA. *Natural Hazards and Earth System Sciences*, 18(11), 3037-3043. <https://doi.org/10.5194/nhess-18-3037-2018>
- 588
- 589 Parlange, J. Y., Lisle, I., Braddock, R. D., & Smith, R. E. (1982). The three-parameter infiltration equation. *Soil Science*,  
590 133(6), 337-341, <https://doi.org/10.1097/00010694-198206000-00001>
- 591 Raymond, C. A., McGuire, L. A., Youberg, A. M., Staley, D. M., & Kean, J. W. (2020). Thresholds for post-wildfire debris  
592 flows: Insights from the Pinal Fire, Arizona, USA. *Earth Surface Processes and Landforms*, 45(6), 1349–1360.  
593 <https://doi.org/10.1002/esp.4805>
- 594 Rengers, F. K., McGuire, L. A., Kean, J. W., Staley, D. M., & Youberg, A. M. (2019). Progress in simplifying hydrologic  
595 model parameterization for broad applications to post-wildfire flooding and debris-flow hazards. In *Earth Surface Processes*  
596 *and Landforms* (Vol. 44, Issue 15, pp. 3078–3092). <https://doi.org/10.1002/esp.4697>
- 597 Saksa, P. C., Bales, R. C., Tobin, B. W., Conklin, M. H., Tague, C. L., & Battles, J. J. (2020). Fuels treatment and wildfire  
598 effects on runoff from Sierra Nevada mixed-conifer forests. *Ecohydrology*, 13, 1–16. <https://doi.org/10.1002/eco.2151>
- 599 Schmidt, K. M., M. N. Hanshaw, J. F. Howle, J. W. Kean, D. M. Staley, J. D. Stock, and G. W. Bawden (2011), Hydrologic  
600 conditions and terrestrial laser scanning of post-fire debris flows in the San Gabriel Mountains, CA, U.S.A., in *Debris-Flow*  
601 *Hazards Mitigation, Mechanics, Prediction, and Assessment*, edited by R. Genevois, D. L. Hamilton, and A. Prestininzi, pp.  
602 583–593, Casa Editrice Univ. La Sapienza, Rome.



- 603 Smith, R. E., Goodrich, D. C., Woolhiser, D. A., & Unkrich, C. L. (1995). KINEROS—A kinematic runoff and erosion model.  
604 In VijayP. Singh (Ed.), *Computer models of watershed hydrology* (p. 1130). Fort Collins, CO: Water Resources Publications.
- 605 Staley, D. M., Kean, J. W., Cannon, S. H., Schmidt, K. M., & Laber, J. L. (2013). Objective definition of rainfall intensity-  
606 duration thresholds for the initiation of post-fire debris flows in southern California. *Landslides*, 10(5), 547–562.  
607 <https://doi.org/10.1007/s10346-012-0341-9>
- 608 Staley, D.M., Wasklewicz, T.A. and Kean, J.W., 2014, Characterizing the primary material sources and dominant erosional  
609 processes for post-fire debris-flow initiation in a headwater basin using multi-temporal terrestrial laser scanning data:  
610 *Geomorphology*, v. 214, 324-338.
- 611 Staley, D. M., Negri, J. A., Kean, J. W., Laber, J. L., Tillery, A. C., & Youberg, A. M. (2017). Prediction of spatially explicit  
612 rainfall intensity–duration thresholds for post-fire debris-flow generation in the western United States. *Geomorphology*, 278,  
613 149–162. <https://doi.org/10.1016/j.geomorph.2016.10.019>
- 614 Stoof, C. R., Vervoort, R. W., Iwema, J., Ferreira, A. J. D., Ritsema, C. J., Group, D., Resources, N., Water, Q., Group, M., &  
615 Green, A. (2012). Hydrological response of a small catchment burned by experimental fire. 267–285.  
616 <https://doi.org/10.5194/hess-16-267-2012>
- 617 Sweeney, T. L. (1992). Modernized areal flash flood guidance. *NOAA Technical Memorandum, NWS HYDRO*, 44.
- 618 Tang, H., McGuire, L. A., Rengers, F. K., Kean, J. W., Staley, D. M., & Smith, J. B. (2019). Evolution of Debris-Flow Initiation  
619 Mechanisms and Sediment Sources During a Sequence of Postwildfire Rainstorms. *Journal of Geophysical Research: Earth  
620 Surface*, 124(6), 1572–1595. <https://doi.org/10.1029/2018JF004837>
- 621 USDA Forest Service (2009). Station fire burned area emergency response (BAER). unpublished Report. Available:  
622 [http://www.fs.usda.gov/Internet/FSE\\_DOCUMENTS/stelprdb5245056.pdf](http://www.fs.usda.gov/Internet/FSE_DOCUMENTS/stelprdb5245056.pdf)
- 623 Watson, C. L., & Letey, J. (1970). Indices for Characterizing Soil-Water Repellency Based upon Contact Angle-Surface  
624 Tension Relationships. *Soil Science Society of America Journal*, 34(6), 841–844.  
625 <https://doi.org/10.2136/sssaj1970.03615995003400060011x>
- 626 Westerling AL, Hidalgo HG, Cayan DR, Swetnam TW. 2006. Warming and earlier spring increase western US forest wildfire  
627 activity. *Science* 313: 940–943.
- 628 Wilson, C., Kampf, S. K., Wagenbrenner, J. W., & Macdonald, L. H. (2018). Forest Ecology and Management Rainfall  
629 thresholds for post- fire runoff and sediment delivery from plot to watershed scales. *Forest Ecology and Management*, 430,  
630 346–356. <https://doi.org/10.1016/j.foreco.2018.08.025>
- 631 Yatheendradas, S., Wagener, T., Gupta, H., Unkrich, C., Goodrich, D., Schaffner, M., & Stewart, A. (2008). Understanding  
632 uncertainty in distributed flash flood forecasting for semiarid regions. *Water Resources Research*, 44(5), 1–17.  
633 <https://doi.org/10.1029/2007WR005940>
- 634 Zhang, J., Howard, K., Langston, C., Kaney, B., Qi, Y., Tang, L., Grams, H., Wang, Y., Cocks, S., Martinaitis, S., Arthur, A.,  
635 Cooper, K., Brogden, J., & Kitzmiller, D. (2016). Multi-Radar Multi-Sensor (MRMS) Quantitative Precipitation Estimation:



- 636 Initial Operating Capabilities, *Bulletin of the American Meteorological Society*, 97(4), 621-638. Retrieved May 23, 2021, from  
637 <https://journals.ametsoc.org/view/journals/bams/97/4/bams-d-14-00174.1.xml>  
638 Zhao, Y., Nearing, M.A., & Guertin, D.P., 2019. A daily spatially explicit stochastic rainfall generator for a semi-arid climate.  
639 *J. Hydrol.* 574, 181–192.